Textured growth of polycrystalline MAX phase carbide coatings via thermal annealing of M/C/Al multilayers

Running title: Textured MAX phase coatings via annealing multilayers

Running Authors: Tang et al.

C. Tang [a)], M. Steinbrück, M. Klimenkov, U. Jäntsch, H.J. Seifert, S. Ulrich, M. Stüber [a)]

Institute for Applied Materials (IAM-AWP), Karlsruhe Institute of Technology (KIT), Hermann-von-Helmholtz-Platz1, 76344 Eggenstein-Leopoldshafen, Germany

[a)] Corresponding authors

Dr. Chongchong Tang
chongchong.tang@kit.edu, phone: +49 (0)721 608 28543, fax: +49 (0)721 608 24567

Dr. Michael Stüber
michael.stueber@kit.edu, phone: +49 (0)721 608 23889, fax: +49 (0)721 608 24567

Highly basal-plane textured and polycrystalline Cr_2AlC, Ti_2AlC and Ti_3AlC_2 single-phase coatings have been successfully synthesized on both amorphous and polycrystalline substrates via controlled thermal annealing of magnetron-sputtered nanoscale multilayers built by individual transition metal, carbon, and aluminum layers. Formation of substitutional solid solution carbide phases was triggered via solid-state diffusion reactions during annealing. Lower-ordered Ti_2AlC 211 MAX phase initially crystallized at intermediate temperature range and was recognized as an intermediate reactant in case of synthesizing Ti_3AlC_2 312 MAX phase via annealing corresponding stoichiometric multilayers. The crystallization onset temperatures identified via *in-situ* high-temperature X-ray diffraction (HTXRD) measurements were approximately 480°C, 660°C and 820°C for Cr_2AlC, Ti_2AlC and Ti_3AlC_2, respectively. Contrary to usually observed columnar structure representative of magnetron-sputtered coatings, the coatings synthesized via the current approach are composed of platelet-like, elongated crystallites. The unique nanoscale multilayered design plays a crucial role in achieving the textured MAX structures during thermal annealing. More specifically, the preferred crystallographic orientation relationships among the as-deposited transition metal layers, the intermediate solid solution phases and the end-product MAX phases facilitate the growth of textured MAX phase films.

I. INTRODUCTION

$M_{n+1}AX_n$ (MAX) phase compounds comprise a large class of layered, hexagonal ternary carbides and nitrides (space group $P6_3/mmc$, 194). Their unique layered and hexagonal crystal structures can be viewed as near-close-packed M layers (M: transition metal) interleaved with pure A-group elemental layer, accompanied by X atoms (X: carbon or nitrogen) filling the M_6X octahedral cages among the M atoms [1–3]. The different n values (typically 1-3) specify the numbers of transition metal carbide and/or nitride layers interleaved with the A elemental layer, denoted 211, 312 and 413 with progressively increasing n values. The covalent-ionic M-X bonds in the MAX phases are exceptionally strong and are comparable to their respective MX binaries; whereas, the metallic M–A bonds are relatively weak [3,4]. Thus, they possess many attractive attributes and properties combining both characteristics of ceramics and metals, originating from the aforementioned unique layered crystal structures and bonding characteristics. For instance, MAX phase compounds exhibit low density, high melting/decomposition points, excellent high-temperature mechanical properties and low thermal expansion coefficients [2,4]. Additionally, unlike common ceramics they are relatively soft and readily machinable, exhibit high thermal and electrical conductivities, good thermal shock and damage tolerance, and occasionally oxidation and fatigue resistance [2,5]. These exceptional properties make MAX phases promising candidate materials for diverse applications in harsh environments as both bulk and thin films [6–8].

Ceramics for engineering applications are frequently deliberately synthesized with a specific preferred crystallographic orientation (sometimes entitled texture-engineered ceramics) [9]. Such ceramics feature enhanced physical and mechanical properties particularly for anisotropic polycrystalline materials [9]. MAX phases unveil highly anisotropic properties owing to their highly-ordered hexagonal crystal structure [2,3,10–13]. Via tailoring the crystallographic texture, superior physical and mechanical properties of bulk MAX phase

materials have been reported compared to their randomly-oriented, polycrystalline forms. For example, enhanced flexural strength and fracture toughness in both parallel and/or perpendicular to the *c*-axis textured direction was achieved for Ti_2AlC, Ti_3AlC_2 [14] and Nb_4AlC_3 [15] MAX phases.

A variety of methods (mainly physical vapor deposition, PVD, and spraying techniques) [16] have been successfully implemented in the last decade allowing to synthesize MAX phases in the form of thin films and coatings at reduced temperatures compared to elevated temperatures required during fabrication of bulk materials. Growth of epitaxial or textured MAX phase thin films (normally below 500 nm thick) has been repeatedly reported on single-crystal substrates [17]. However, fabrication of thick MAX phase coatings (at least few microns thick) on amorphous or polycrystalline substrates, specifically technically-relevant substrates, regularly results in coatings with randomly oriented, polycrystalline microstructure [18–22]. Experimental investigations and theoretical calculations have demonstrated that basal-plane textured MAX phase coatings are preferred with respect to applications in tribology [23], corrosion protection [24,25] and as diffusion barrier [26,27]. For instance, anisotropic corrosion performances with preferential dissolution of the A-elemental layer were seen for Ti_2AlC, Ti_3AlC_2 and Ti_3SiC_2 during hydrothermal corrosion tests [7]. The *c*-axis textured samples or grains exhibit higher resistance to hydrothermal corrosion. Additional investigations indicate that a dense, basal-plane textured MAX phase coating could act as a diffusion barrier against interstitial H atoms [28]. The underlying mechanisms are mainly involved in the high chemical activity and mobility of the A element atoms in the MAX phase structures. In addition, similar enhanced mechanical properties are anticipated in case of textured MAX phase films or coatings with desired crystallographic orientation as evidenced for bulk materials. Synthesis of single-phase MAX phase coatings additionally remains a challenging issue owing to their highly ordered crystal structures and potential growth of many competitive compounds (typically intermetallic phases and binary ceramics)

[16]. Thus, syntheses of single-phase and highly textured MAX phase coatings are critical for exploring their anisotropic physical properties and broadening their technological applications.

Recently, we demonstrated that via controlled thermal annealing of specially-designed nanoscale-multilayers deposited by magnetron sputtering from elemental targets textured and phase-pure Ti_2AlC coatings can be realized on different types of substrates, including amorphous SiO_2/Si and polycrystalline zirconium alloy [29,30]. Following a similar approach, Gröner et al. have successfully prepared basal-plane oriented Ti_2AlN MAX phase coatings on polycrystalline Al_2O_3 substrates by annealing Ti/AlN multilayers [31]. Controlled thermal annealing of nanostructured multilayer system has emerged as a promising and facile synthesis method for textured and polycrystalline MAX phase coatings [32,33] and a potential alternative route for other complex compounds [34]. However, only a small number of MAX phase coatings have been explored and realized via this approach. Additionally, it appears also not applicable for certain ternary systems. For instance, crystallization of a cubic, solid solution Zr(Al)C phase with a B1 NaCl crystal structure rather than Zr_2AlC MAX phase via annealing of Zr/C/Al multilayers has been observed in our previous studies [35]. The reaction mechanisms, phase formation paths, and crystallographic orientation evolutions during annealing of such multilayered stacks are still lack of scientific understanding, which hinder the optimization and application of the process.

In this study, we extend this approach to synthesize coatings of three MAX phase carbides in two ternary systems, with particular emphasis on one higher-ordered 312 MAX phase (Ti_3AlC_2), on various substrates. These Al-containing MAX phase carbides possess excellent oxidation resistance with autonomous self-healing capability, revealing promising prospects for high-temperature applications [5,36,37]. Specifically, textured growth of the higher-ordered 312 phase coatings on polycrystalline substrates has been rarely reported. This study intends to contribute and enhance our understanding of underlying mechanisms for textured

growth of MAX phase coatings during the thermal annealing process. The microstructure evolution and phase formation as a function of annealing temperature were systematically investigated by *in-situ* high-temperature X-ray diffraction (HTXRD), Raman spectroscopy and high resolution transmission electron microscopy (HRTEM). The phase formation paths and fundamental mechanisms contributing to growth of the textured 211 and 312 MAX phase coatings are comparatively investigated and discussed.

II. EXPERIMENTAL

The MAX phase coatings presented in this study were synthesized via a two-step process, specifically deposition of nanoscale elemental M/C/Al multilayers via magnetron sputtering and subsequent *ex-situ* thermal annealing in argon (6N). The multilayers were deposited onto plate Si(100) wafer, Si wafer with thermally grown amorphous SiO_2 layer, SiO_2/Si, and polycrystalline Al_2O_3 substrates (MTI Corporation, USA) using a laboratory PVD equipment (Leybold Z 550 coater) from three elemental targets (i.e. transition metal, graphite and aluminum). The size of the substrates is $0.375 – 0.5 \times 10 \times 10$ mm^3. The substrates were washed ultrasonically in acetone for 10 min before being introduced in the vacuum chamber. They were placed on a rotating sample holder at a vertical distance of around 7 cm to the sputtering targets inside the chamber. After evacuation of the chamber to a base pressure of around 1×10^{-4} Pa, the substrates were plasma-etched in pure Ar atmosphere with a gas pressure of 0.5 Pa and RF power of 500 W for 10 min.

The design of the nanoscale elemental multilayers was done according to these considerations: chemical compositions of the multilayers corresponding to three intended MAX phases were examined, namely two 211 phases, Cr_2AlC and Ti_2AlC, and one higher ordered 312 phase Ti_3AlC_2. The elemental multilayers were designed with a periodically repeated stacking sequence of transition metal, graphite and aluminum. The thicknesses of the individual elemental layers were calculated according to their stoichiometric ratio (2:1:1 or

3:1:2) and considering their theoretical densities. The thickest elemental layer (transition metal layer) was restricted to approximately 10 nm to warrant a short diffusion length during crystallization of MAX phases via subsequent annealing. Fig. 1 displays the schematic illustration of one multilayer stack and anticipated thickness of each individual sublayer within the three multilayer designs. The multilayered stacks were repeated until the coating thicknesses reached a value around 3.5 μm.

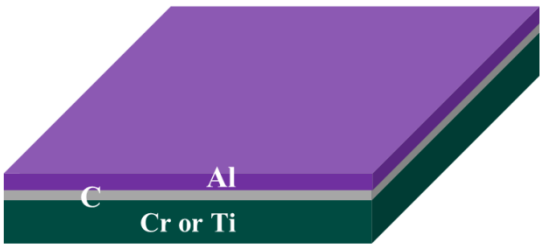

Design	Thickness (nm)
Cr/C/Al (2:1:1)	~7.2/2.6/4.9
Ti/C/Al (2:1:1)	~8.8/2.2/4.1
Ti/C/Al (3:2:1)	~12.0/4.0/3.8

FIG. 1. Schematic illustration of one multilayer stack and anticipated thickness of each individual sublayer within the three multilayer designs.

All power was maintained at ~200 W for the three targets during deposition, with RF mode operation for the transition metal and aluminum targets and DC mode operation for the graphite target. The working pressure of the argon gas was 0.5 Pa. The substrates were grounded and not intentionally heated. Above configurations were initially used in separate experiments to deposit individual transition metal, carbon, and aluminum single layer films on Si substrates, aiming to determinate the growth rate of each individual layer material. To achieve the desired multilayer design, the sample holder was operated in a stop-and-go mode during deposition, i.e. the sample holder rotated from one target position to another one and stayed for various holding times at each individual target position. More detailed information

on the deposition of such multilayers can be found in [29,30]. After deposition, the as-deposited multilayers were annealed in pure Ar at atmospheric pressure using a commercial thermal balance (NETZSCH STA-449 F3 Jupiter) to facilitate the growth of MAX phases via solid state reactions. The annealing temperatures were selected based on *in-situ* HTXRD measurements and varied from 400°C to 1000°C depending on the three designs. The isothermal dwell time was typically maintained at 10 min and the heating and the cooling rates were fixed at 10 K/min.

The chemical compositions of the as-deposited coatings on Si wafer were measured via a field-emission electron probe micro-analyzer (EPMA, JEOL JXA-8530F). An average value based on at least four measurements located in different surface areas was provided. *In-situ* HTXRD (Bruker D8) and *ex-situ* classical XRD (Seifert PAD II) measurements have been performed to unravel the phase evolution of the coatings during or after annealing. *In-situ* XRD patterns were acquired from 300°C or 400°C to 1000°C in a Bragg-Brentano configuration using an Anton Paar HTK1200N high temperature stage with Cu Kα1 radiation (λ=0.15406 nm) operating at 40 kV and 40 mA. A temperature step of 20 K and a heating rate of 30 K/min between each temperature step were applied. The samples were heated in a pure Ar atmosphere. The recorded 2θ range was from 8° to 50° with a step size of 0.04°, and duration of each scan was approximately 5 min. These conditions were chosen to allow us to probe the most intense reflections and the phase evolution at narrow temperature interval. The *ex-situ* XRD measurements were also implemented in Bragg-Brentano geometry (θ-2θ) with a step size of 0.002 ° and a scan speed at 1 °/min. Raman spectroscopy analysis was also conducted on some specific samples. The Raman spectra were collected and recorded between 160 and 2000 cm^{-1} wavelength using an argon ion laser of 514.5 nm wavelength (Renishaw 1000 micro spectrometer) and 2~3 mW power on the sample surface. Microstructural and compositional analyses of selected coating samples were carried out with high-resolution transmission electron microscopy (HRTEM, FEI Tecnai 20 FEG) using an

accelerating voltage of 200 kV. The cross-sectional lamellas for HRTEM analyses were prepared by focused ion beam (FIB) *in-situ* lift-out technique. The lamellas were thinned using ion milling to achieve sufficient electron transparency.

III. RESULTS

A. As-deposited coatings

The chemical compositions of the as-deposited coatings via EPMA measurements are summarized in Table I. Average values of the atomic concentrations of each element are anticipated considering only few nanometer thickness of each sublayer within the multilayered stacks (see Fig. 2). As shown in Table I, the atomic concentrations of all as-deposited coatings are similar to the desired theoretical concentration values of the intended MAX phases; especially the concentration ratios of transition metal (Cr or Ti) : aluminum coincide nearly ideally with the desired stoichiometric ratios of the corresponding MAX phases for all three as-deposited coatings. However, the carbon concentrations of all coatings are lower than the expected theoretical values (25.0 or 33.3 at.%). One reasonable interpretation is that the density of the deposited (amorphous) carbon layer is typically lower than the theoretical density of (crystalline) graphite applied initially to determine the required single layer thickness [29]. Further, the sputter deposition of amorphous carbon thin films at low target power is related with extremely slow growth rates. Considering the nanoscale multilayered structure and the required thickness of an individual carbon layer in these stacks, it is reasonable that a small error in thickness per layer sums up within the numerous multilayers and results in this larger deviation from a perfect stoichiometry. Similarly, the concentrations of Cr or Ti are slightly larger in comparison with the theoretical values; only in case of the Ti/C/Al multilayer with 2:1:1 MAX phase pre-design, the concentration of the M element is exactly 50 at.%. A minor amount of oxygen appears to be incorporated into the coatings during growth, with a fairly higher quantity for Ti-based coatings. Since experimentally synthesized MAX phase compounds routinely comprise (accommodate)

substantial carbon and/or nitrogen vacancies and interstitial oxygen can substitute for carbon and/or nitrogen in MAX phase structures [16,38,39], these phenomena (C-deficiencies and oxygen impurities) should not adversely affect the crystallization behavior of MAX phases upon annealing of the multilayers.

TABLE I. Chemical composition of the three as-deposited coatings measured by EPMA

Coating design	**Intended MAX phase**	**Cr (at.%)**	**Ti (at.%)**	**C (at.%)**	**Al (at.%)**	**O (at.%)**	**M:Al ratio**
Cr/C/Al (2:1:1)	Cr_2AlC	54.5	—	19.1	26.1	0.3	2.08
Ti/C/Al (2:1:1)	Ti_2AlC	—	50.8	21.9	26.0	1.3	1.95
Ti/C/Al (3:2:1)	Ti_3AlC_2	—	54.2	26.5	17.5	1.7	3.09

Fig. 2 illustrates the typical multilayered design of an as-deposited Ti/C/Al (2:1:1) coating on Si substrate as an example. The periodically multilayered stacks consisting of nanoscale individual elemental sublayers in the as-deposited coatings are clearly visible in Fig. 2. The thicknesses of each sublayer are in line with estimated values based on the pre-determined deposition rates of the individual targets. The thickest sublayer in Fig. 2, i.e. the transition metal layer (Ti), is approximately 9 nm thick. There is obviously no substantial intermixing between each sublayer and the interfaces are easily visible as revealed in the inserted, high-magnification TEM image. As expected, the carbon layers are amorphous; whereas, the two metallic layers are composed of nanocrystals.

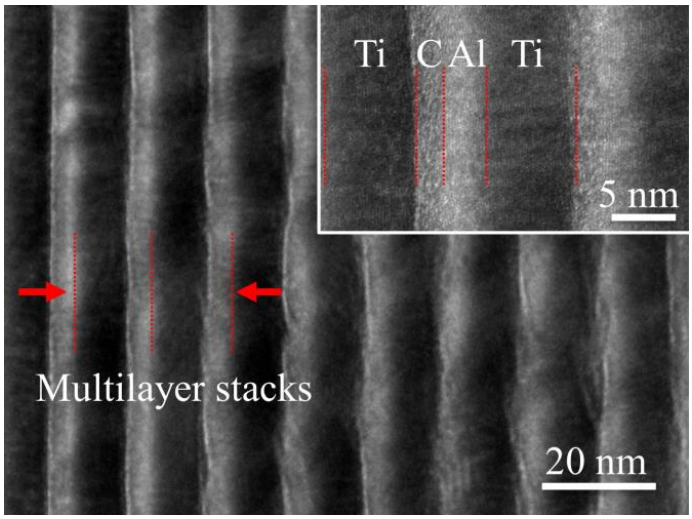

FIG. 2. Bright-field TEM images of the as-deposited Ti/C/Al (2:1:1) coating displaying the multilayered architecture within nanoscale elemental sublayers.

B. *Annealed coatings*

In this section the results of the different annealing experiments (according to the description in section 2) are presented with a focus on the intended MAX phase structures. First, the coatings with 2:1:1 MAX phase designs are considered. Afterwards, coatings with an intended 3:1:2 MAX phase design are addressed.

1. *Cr_2AlC coatings*

The crystallization behavior and phase evolution as a function of annealing temperature examined by *in-situ* HTXRD of the Cr/C/Al (2:1:1) coating on polycrystalline Al_2O_3 substrates are shown in Fig. 3. Fig. 4 displays the *ex-situ* XRD patterns obtained in separate annealing experiments using individual coating samples at three different temperatures. Fig. 3 (a) presents an overview of the diffractograms of a Cr/C/Al (2:1:1) coating over the full annealing temperature range from 300°C to 1000°C, while Fig. 3 (b) shows the diffractograms in more detail over the temperature range 300°C to 500°C, where essential crystallization processes were observed. The diffractograms (at 300°C in Fig. 3 and Fig. 4) indicate a preferred crystallographic orientation of the transition metal layer, namely Cr (110), in the as-deposited coatings. In Fig. 3 (b) the theoretically expected positions of Cr (110) and Al (111) according to JCPDS cards #06-0694 and #04-0787 are marked by dashed

lines. The Cr (110) reflections are relatively broad (with a full width at half maximum (FWHM) ~2.2° at 300°C), indicating the nanocrystalline nature of the Cr layers. The estimated grain size is ~ 4 nm based on Scherrer equation. Diffraction intensities of the Al layers cannot be clearly identified, due to the low thickness of the Al layers in the multilayered stacks and short probe time. The Cr reflection shows an asymmetric shoulder at lower diffraction angle, i.e. around the position of the Al (111) reflection. Diffraction signals attributable to the alumina substrate are marked by "S".

At lower annealing temperatures (approximately up to 360°C), the diffractograms of the coating and the positions of their reflections remain barely unchanged, indicating that the elemental multilayered architecture sustains its integrity and remains stable. Then, with annealing temperatures in the range 380°C to 460°C, first signs of new phase formation are observed: the Cr (110) reflection is clearly broadening with a more pronounced shoulder formation at lower diffraction angle (up to a temperature of 420°C) and then gradually shifting to lower diffraction angles and becoming more symmetric (at annealing temperatures 440°C - 460°C). This relatively broad reflection centered at ~42.5° in Fig. 3 (b) is close to the position of the 2θ value characteristic of the (101) lattice plane of Cr_2C (JCPDS #14-0519). No noticeable diffraction signal belonging to Cr-Al intermetallic compounds was detected. Thus, the formation of a substitutional solid solution hexagonal-$(CrAl)_2C_x$ phase [40,41] via solid-state diffusion reactions may be proposed here .

As the temperature increases further, nucleation and enhanced crystallization of a Cr_2AlC MAX phase (JCPDS #29-0017) was undoubtedly confirmed via identification of its specific reflection of the (002) lattice plane at low diffraction angle. An annealing temperature of 480°C - 500°C results in a further, moderate shift of the above described reflection to lower diffraction angle, ~42.1°. While, simultaneously a second diffraction signal around a 2θ value of ~13.7° appears. The intensities of these two diffraction signals increase during annealing at 500°C, while the FWHM values decrease and the reflections get more symmetric. These two

diffraction signals can be attributed to the Cr_2AlC MAX phase structure. The intensities of the reflection of the Cr_2AlC (002) lattice plane increases upon further annealing above 500°C. The microstructure of the coating does not change anymore during annealing up to 1000°C.

The *ex-situ* XRD diffractogram of the as-deposited coating presented in Fig. 4 additionally confirms the (110) preferred crystallographic orientation of the Cr layer. The Al (111) reflection can be resolved somehow now due to the relatively longer probe time. The phase evolution and associated crystallization temperature after annealing are consistent with the findings revealed by the in-situ HTXRD measurements. One difference is that two well-separated and broad reflections were observed after annealing at 450°C. The broad signals at 2θ about 41.5° and 43.7° most probably originated from the Al_9Cr_4 (330) reflection (JCPDS #44-1294) and the Cr_7C_3 (151) reflection (JCPDS #44-1294), respectively. The formation of Cr-Al intermetallic compounds and chromium carbides most likely correlates with phase dissociation during the cooling period and will be discussed later. Annealing at 500°C already triggered the crystallization of the Cr_2AlC MAX phase (more specifically, ~480°C resolved in HTXRD). Formation of a phase-pure Cr_2AlC MAX phase was confirmed after annealing at 550°C for 10 min. The broad feature of its diffraction peaks indicated the weak degree of crystallinity and fine grain size considering the relatively low annealing temperature and short dwell time of 10 minutes herein.

Additionally, all diffraction peaks correlated with Cr_2AlC both in HTXRD and XRD diffractograms coincide with the reflection of its {00l} basal planes, indicating that the Cr_2AlC coatings possess a basal-plane preferred orientation after annealing.

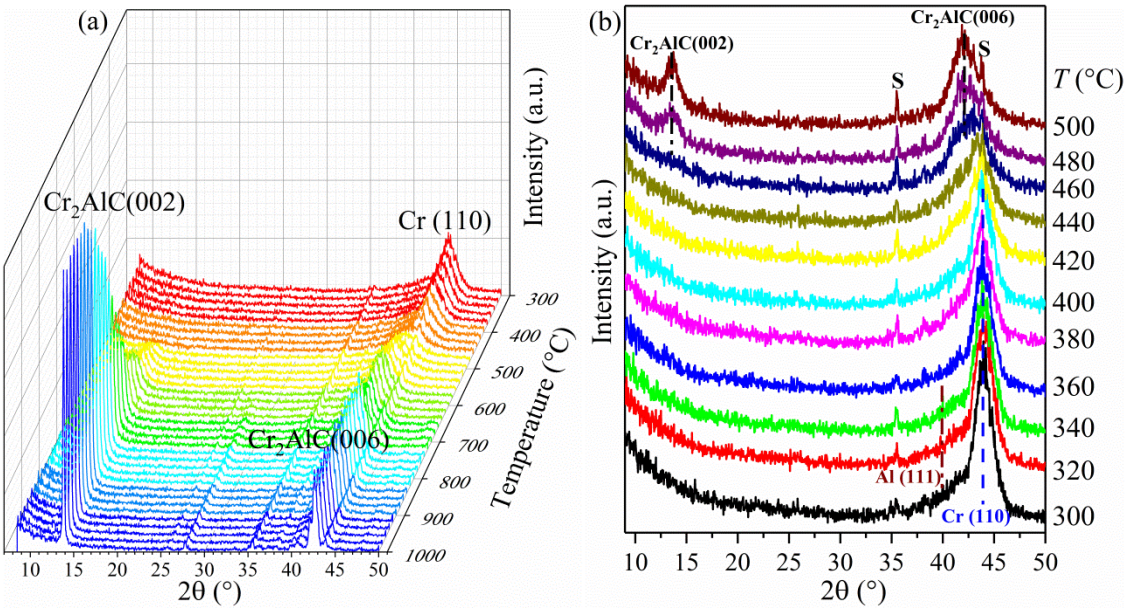

FIG. 3. In-situ HTXRD patterns of a Cr/C/Al (2:1:1) coating on polycrystalline Al_2O_3 substrate during annealing in argon. (a) multiple plots of diffractograms over the full temperature range from 300°C to 1000°C ; (b) detailed overview of diffractograms over a selected temperature interval 300°C to 500°C. S represents diffraction signals of the alumina substrate.

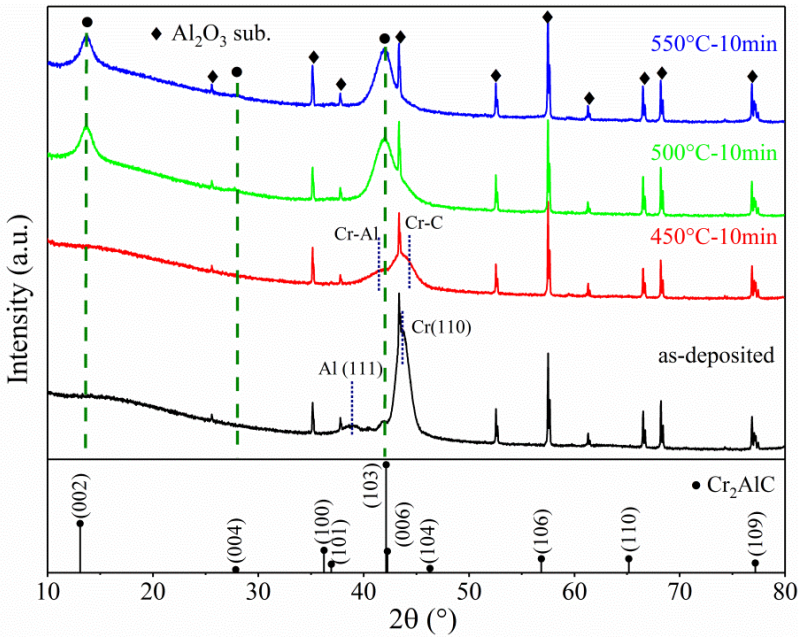

FIG. 4 XRD patterns of the Cr/C/Al coatings on Al_2O_3 substrates after annealing at given temperatures. The black circle and the black star symbols represent Cr_2AlC and Al_2O_3 substrate, respectively.

2. Ti_2AlC coatings

Fig. 5 (a) presents an overview of the diffractograms of a Ti/C/Al (2:1:1) coating over the full annealing temperature range from 300°C to 1000°C. Fig. 5 (b) and (c) show the diffractograms in more detail over the temperature ranges 300°C to 500°C, and 520°C to 800°C, where different crystallization processes were observed. Reflections of the alumina substrate are marked by "S" again.

At an annealing temperature of 300°C the diffractogram indicates a preferred crystallographic orientation of the transition metal layer, now Ti (002) (JCPDS # 05-0682). The reflection has a FWHM of 1.32°, suggesting a crystallite size of the Ti layers of ~7 nm. Again, no diffraction intensities of the Al layers can be clearly identified. One additional reason except the aforementioned ones for its absence is the diffraction peaks from Ti (002) and Al (111) planes (< 1% difference) closely overlap with each other. At lower annealing temperatures (approximately up to 420°C), the diffractograms of the coating and the positions of their reflection remain unchanged, suggesting that the elemental multilayered architecture retains its integrity and remains stable. The symmetric reflection of the Ti (002) lattice plane is only very little broadening with increasing temperature, while the effect becomes more visible at 420°C. With further increase of the annealing temperatures in the range 440°C to 500°C, first effects of new phase formation are observed: the Ti (002) reflection is clearly shifting towards lower diffraction angles, it is broadening and its intensity is decreasing. In Fig. 5 (b) a dashed line corresponding with the reflection position of the (111) lattice plane of TiC_x (JCPDS # 32-1383) is marked. The relatively broad reflections of the 440°C-500°C annealed coating centered at ~35.5° in Fig. 5 (b) is observed around this position, and it shifts towards this position with increasing temperature. No noticeable diffraction signal attributable to Ti-Al intermetallic compounds was detected. Thus, the formation of a substitutional solid

solution cubic-(TiAl)C_x phase [42–44] via solid-state diffusion reactions may be proposed in this case.

A further increase of the annealing temperature leads to a second, significant change in microstructure evolution. In the range 520°C – 640°C the before mentioned reflection attributed to a (TiAl)C_x solid solution is significantly shifting to larger diffraction angles, accompanied by a change in its shape. At an annealing temperature of ~ 660°C crystallization onset of a Ti_2AlC MAX phase (JCPDS #29-0095) can be observed; the nucleation and enhanced crystallization of the Ti_2AlC MAX phase was undoubtedly confirmed by identifying its specific reflection of (002) lattice plane at low diffraction angle, ~12.9°. Increasing the annealing temperature up to 1000°C results in diffractograms showing sharp diffraction signals characteristic of the MAX phase structure of (00l) lattice planes only. Growth of a highly basal-plane textured MAX phase coating is thus evidenced. The crystallinity of the MAX phase grains is progressively enhanced with increasing annealing temperatures. It is noteworthy that the intensities of the reflections originating from the Ti_2AlC coating decreased at temperatures higher than 900°C, probably owing to its relatively low stability and vulnerability to decomposition/oxidation at elevated temperatures such as reported previously for MAX phase coatings deposited via PVD [45,46].

The *ex-situ* XRD patterns of identical coatings obtained in separate annealing experiments are presented in Fig. 6. The preferred crystallographic orientation, phase evolution and associated crystallization temperature are consistent with the *in-situ* HTXRD results. In the as-deposited coatings, the Ti layers are featured by a basal-plane, i.e. (002) preferred orientation. Similarly to the Cr/C/Al coatings, annealing at an intermediate temperature of 600°C for 10 min with subsequent cooling results in the formation of a mixture of TiC and intermetallic Ti-Al phases. The two broad diffraction peaks located at around 36.8° and 39.0° can be assigned to TiC_x (110) and Al_3Ti (118)(JCPDS #26-0038), respectively. The predominant phase turns into Ti_2AlC with some unreacted, residual

intermediate phases after annealing at 700°C for 10 min. The elemental multilayers transformed to a single Ti_2AlC MAX phase with the basal-plane preferred orientation after annealing at 800°C for 10 min, as shown in Fig. 6.

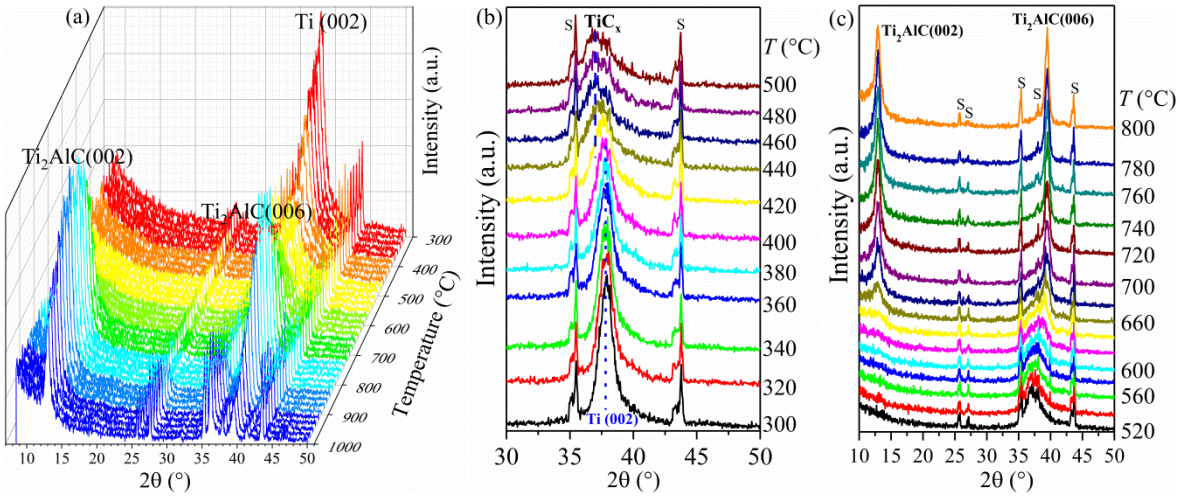

FIG. 5. In-situ HTXRD patterns of a Ti/C/Al (2:1:1) coating on polycrystalline Al_2O_3 substrate during annealing in argon. (a) multiple plots of diffractograms over the full temperature range from 300°C to 1000°C; detailed overview of diffractograms over a selected temperature interval (b) from 300°C to 500°C and (c) from 520°C to 800°C. S represents diffraction signals of the alumina substrate.

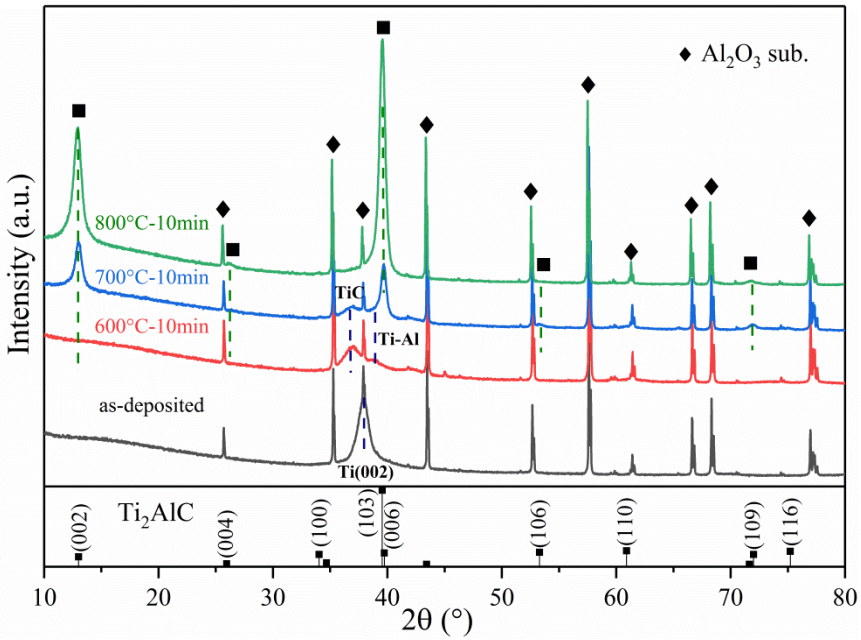

FIG. 6. XRD patterns of the Ti/C/Al coatings (2:1:1) on Al_2O_3 substrates after annealing at given temperatures. The black square and the black star symbols represent Ti_2AlC and Al_2O_3 substrate, respectively.

3. Ti_3AlC_2 coatings

The *in-situ* HTXRD patterns of a Ti/C/Al (3:2:1) coating on polycrystalline Al_2O_3 substrate are displayed in

Fig. 7. Several steps of microstructure evolution and phase formation are observed. Similar to the previously discussed results for Ti/C/Al (2:1:1) coatings, the diffractograms at intermediate temperatures (~ 460°C-660°C) suggest the growth of a metastable $(TiAl)C_x$ solid solution phase (while for the as-deposited and 400-460°C annealed coating only reflections of the (002) lattice plane of pure Ti were observed,

Fig. 7 (a)). Independent of the specific multilayer design of the Ti/C/Al (3:2:1) coating, no direct nucleation of the highly-ordered 312 MAX phase is observed; instead, the lower-ordered Ti_2AlC 211 MAX phase initially crystallized starting from ~680°C (

Fig. 7 (b)). The crystallization onset temperature of the Ti_3AlC_2 MAX phase (JCPDS #52-0875) was identified at ~820°C. The two MAX phases obviously co-exist in the temperature range of 820°C to ~ 900°C. The relatively broad diffraction reflex at 2θ of ~12.8° assigned to the Ti_2AlC (002) lattice plane indicates the low crystallinity of the 211 MAX phase, and its crystallinity is not noticeably changed during annealing up to 900°C. Above 900°C, the Ti_2AlC phase completely vanished and only diffraction reflexes of the Ti_3AlC_2 phase were detected. The improved ordering of the Ti_3AlC_2 structure with increasing annealing temperature was recognized by the higher intensity and lower FWHM values of the (002) reflection. In addition, the substantially high intensities of the diffraction peaks originating from the basal planes, i.e. (002), (004) and (006), of the hexagonal crystals again suggest a highly textured microstructure of the annealed coating.

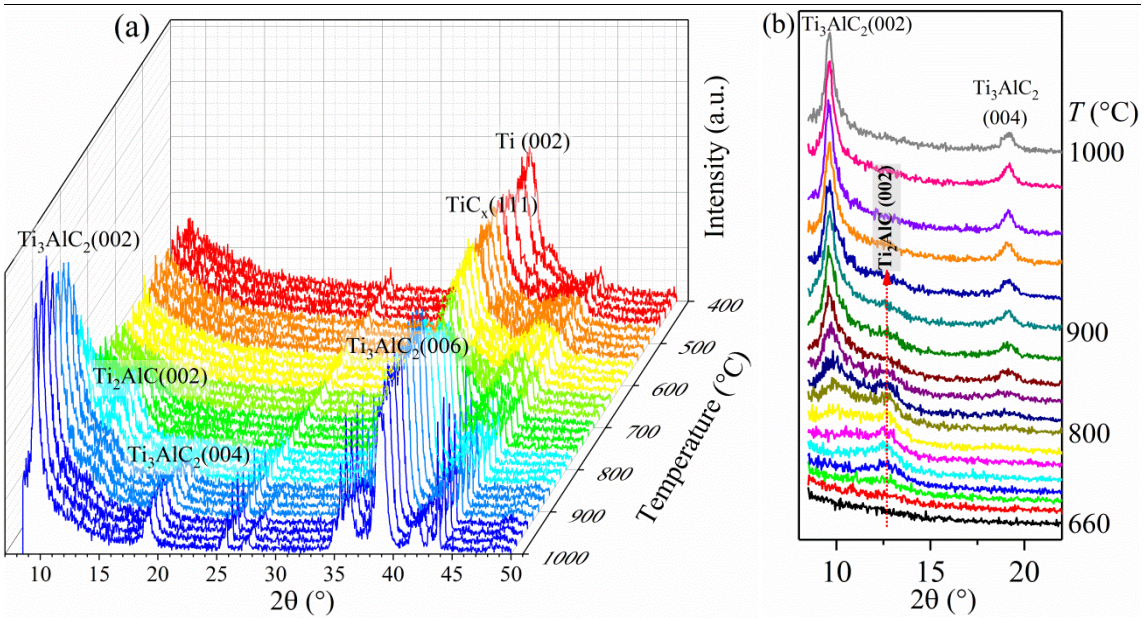

FIG. 7. In-situ HTXRD patterns of a Ti/C/Al (3:2:1) coating on polycrystalline Al_2O_3 substrate during annealing in argon. (a) multiple plots of diffractograms over the full temperature range from 400°C to 1000°C; (b) detailed overview of diffractograms over a selected interesting temperature interval from 660°C to 1000°C.

To further elucidate the phase evolution route during synthesis of the highly-ordered 312 MAX phase, separate annealing experiments using individual samples were performed at different temperatures from 800°C to 1000°C. XRD and Raman spectroscopy analyses were carried out after the annealing; the results are presented in Fig. 8 and Fig. 9, respectively. Fig. 8 shows the XRD patterns of the as-deposited and annealed Ti/C/Al (3:2:1) coatings on polycrystalline Al_2O_3 substrate (similar results were obtained for the as-deposited and annealed multilayers on amorphous SiO_2/Si substrates and are not shown here). Expected and measured 2θ positions of the sapphire substrate (marked by dark diamond symbols) and the Ti_2AlC (marked by dark square symbols) and Ti_3AlC_2 MAX phases (marked by dark inverted triangle symbols) are indicated with their lattice plane assignments. Furthermore, the diffraction signals of Ti and TiC_x phases are indicated. As can be seen, the titanium layers exhibit a (002) preferred crystallographic orientation in the as-deposited coatings as aforementioned. The low intensity Bragg reflection of the expected Al (111) lattice plane (at 2θ of ~38.5°) overlaps with the diffraction reflection of the Ti (002) lattice plane and is hardly

discernible. After annealing at 800°C for 10 min, the multilayers transformed to a composite being composed of a mixture of Ti_2AlC and TiC_x (or solid solution $(TiAl)C_x$) phases. The diffraction reflections at 2θ values of ~12.9°, 39.6° and 36.8° can be assigned to the (002) and (006) lattice planes of Ti_2AlC and the TiC_x (111) lattice plane, respectively. The shifting of the TiC_x (111) reflection to higher value compared with the theoretical value (35.9°) presumably arises from the non-ideal stoichiometric ratio and incorporation of Al atoms. The broad feature of their diffraction peaks indicates the poor degree of crystallinity of both phases. Annealing at 900°C (with 10 min holding time) already activated the crystallization of the Ti_3AlC_2 MAX phase. The specific Bragg reflection at 2θ of 9.5° could be unambiguously assigned to the Ti_3AlC_2 (002) lattice plane. Moreover, the peak at 2θ of 36.8° moves to a lower angle owing to the contribution from the Ti_3AlC_2 (006) reflection. These findings are consistent with the crystallization behavior revealed by the *in-situ* HTXRD studies above.

Annealing the coating for 10 minutes at 1000°C resulted in a considerable increase of the intensities of the Bragg reflections originating from the Ti_3AlC_2 MAX phase (accompanied by a narrowing of the FWHM value of the (002) diffraction reflection and the appearance of the diffraction reflection of (004) lattice plane). However, even though the diffraction signals attributed to the Ti_2AlC and TiC_x phases show lower intensities simultaneously, they were still detectable by XRD after annealing for 10 min. The short annealing period here did obviously not permit the complete transformation from the intermediate phases to the Ti_3AlC_2 phase via diffusion reactions. By extending the annealing time to 30 min, the intermediate phases were not detected anymore and a phase-pure Ti_3AlC_2 coating was successfully synthesized. The intensity of the diffraction peak stemming from the Ti_3AlC_2 (002) lattice plane increased by ~two times while the FWHM only decreased by ~10%, indicating improved crystallinity and only moderate grain growth. Furthermore, all major diffraction signals identified now coincided with the peak positions of {00l} basal planes, except of three signals of significantly lower intensities, attributable to (105), (109)

and (118) lattice planes. The Lorentz orientation factor (f_L) [12,14], which is regularly utilized to evaluate the degree of texture, calculated for the preferred orientation along the *c*-axis $f_{(00l)}$ reaches 0.93 (1 for single crystal). The Ti_3AlC_2 coatings, consequently, are exclusively constituted of highly basal-plane textured polycrystals and their {00l} basal planes are aligned parallel to the substrate surface and previously as-deposited multilayers.

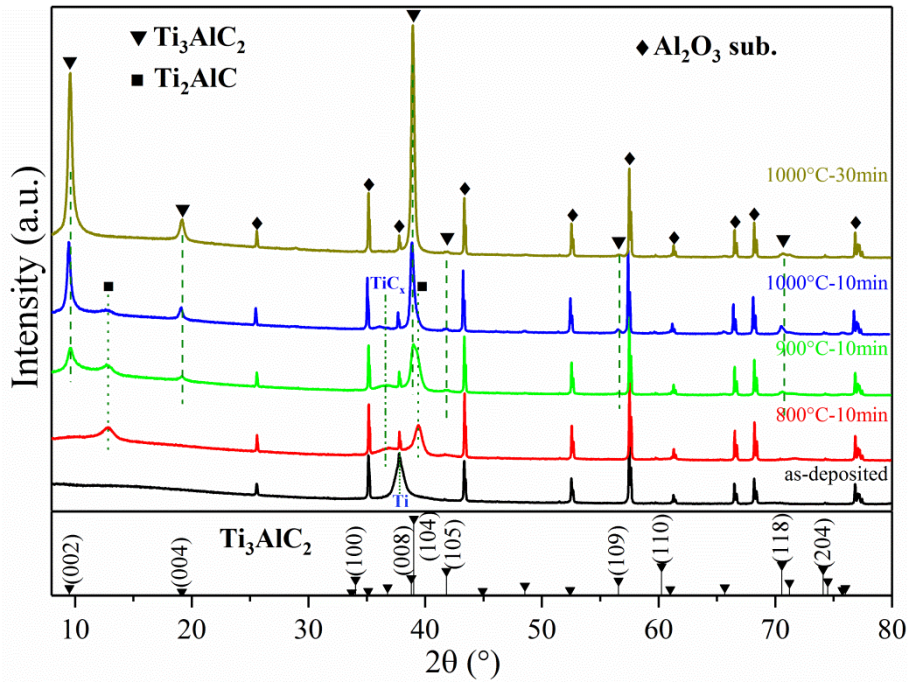

FIG. 8. XRD patterns of as-deposited and annealed Ti/C/Al (3:2:1) coatings on polycrystalline Al_2O_3 substrate. The black square, the black triangle and the black star symbols represent Ti_2AlC, $Ti3AlC_2$ and Al_2O_3 substrate, respectively.

Raman spectroscopy analyses (Fig. 9) further confirmed the interpretations of the crystallization behavior and phase evolution during annealing of the Ti/C/Al (3:2:1) coatings at successively increasing temperatures. In Fig. 9, the theoretical Raman vibration modes of carbon (marked by black dashed lines), Ti_2AlC (marked by brown dashed lines) and Ti_3AlC_2 (marked by blue dashed lines) are indicated. In case of the as-deposited multilayer coatings no obvious signal was recorded except the so-called D and G bands generated by amorphous or disordered carbon-containing materials (i.e. in the wavenumber region 1200-1600 cm^{-1}). This

again indicates that the magnetron sputtered carbon layers are grown in an amorphous state. The theoretical Raman vibration modes E_{1g}&E_{2g} and A_{1g} (vibrational direction parallel or perpendicular to the basal plane, respectively) at low wavenumbers of Ti_2AlC are located at 265&266 cm^{-1} and 365 cm^{-1}, while those of Ti_3AlC_2 are located at 182&197 cm^{-1} and 268 cm^{-1} [47,48]. Considering the Raman spectra of the annealed coatings, some essential differences can be observed: annealing the coating at 800°C for 10 minutes results in the indication of two broader bands around the positons of the E_{1g}&E_{2g} and A_{1g} of Ti_2AlC, while simultaneously the characteristic band of the amorphous carbon phase starts to develop two more separated signals, i.e. formation of more pronounced D and G bands. This suggests atomic re-arrangement events, contributing to the growth of intermediate, low-crystalline $(TiAl)C_x$ and Ti_2AlC phases, and tendency to graphitization of the remaining carbon phase. Annealing a coating at 900°C for 10 minutes supports the formation of both Ti_2AlC and Ti_3AlC_2 phases (now clearly visible by the E_{2g} and A_{1g} vibrational modes of Ti_3AlC_2), while the character of the carbon signals does not change further (while their intensities are reduced in comparison to the 800°C 10 min annealed coating). Note that the amorphous/disordered carbon feature completely disappeared in the Raman spectrum when a coating was annealed for 10 minutes at 1000°C. In this case, the Raman peaks assigned to Ti_2AlC became nearly invisible, and only (relatively broad) bands attributable to the Ti_3AlC_2 MAX phase are observed. This reveals that the solid-state reaction within the two intermediate phases resulted in the growth of the higher-ordered Ti_3AlC_2 phase, and the carbon phase was completely consumed during this microstructure formation. The Raman signals attributed to the Ti_3AlC_2 phase get narrower and stronger with annealing time extended to 30 min, and the locations of these signals fits well with the calculated theoretical values as mentioned above.

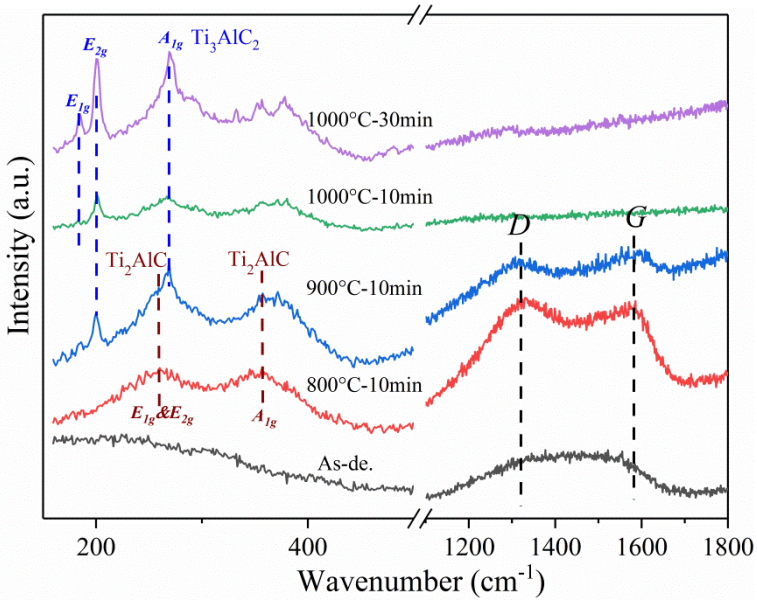

FIG. 9. Raman spectra of as-deposited and annealed Ti/C/Al (3:2:1) coatings on polycrystalline Al_2O_3 substrate.

The microstructure of the Ti_3AlC_2 coating annealed at 1000°C for 30 min was characterized by HRTEM; a cross-sectional bright field overview image and two high magnification bright field images highlighting the grains and lattice structure with one Fast Fourier Transform (FFT) analysis are presented in Fig. 10. It can be seen in Fig. 10 (a), that the coating possesses a compact structure in the bulk and is free of any noticeable macro-size growth defects. The thickness of the coating is around 3.6 µm. Different from a columnar structure, which is typically reported for MAX phase coatings deposited by co-sputtering or compound sputtering via intentional heating of the substrate, the coating synthesized in this study clearly constitutes of platelet-like, elongated grains (Fig. 10 (b)). The average grain sizes are ~200 nm in length and ~30 nm in width (some grains are highlighted in Fig. 10 (b)). No evidence for the growth of common impurity phases (especially binary intermetallic and titanium carbide phases) within the coating and at coating/substrate interface is found, Fig. 10 (b) and (c). The growth of polycrystalline and highly *c*-axis textured Ti_3AlC_2 grains can be clearly seen; while individual grains are slightly tilted to the interface (which may partially be attributed to relatively high roughness of the substrate). The representative nano-layered crystal structure of the Ti_3AlC_2 MAX phase was revealed and the measured d-spacing of the

(002) lattice planes is ~0.92 nm, in excellent coherency with the theoretical value as illustrated in Fig. 10 (c). The typical (00l) diffraction spots of the MAX phase can be easily identified on the FFT image in Fig. 10 (d).

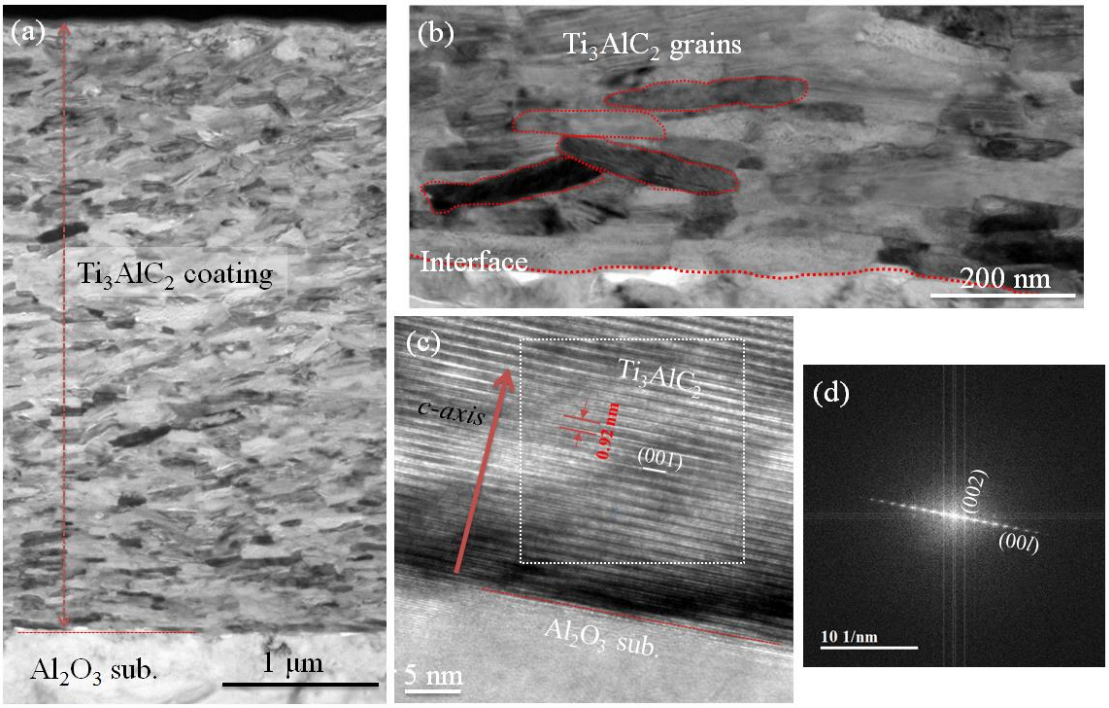

FIG. 10 TEM characterization of the Ti_3AlC_2 coating on polycrystalline Al_2O_3 substrate annealed at 1000°C for 30 min. (a) An TEM cross-sectional bright field overview image of the coating, high magnification bright field images highlighting (b) the grains and (c) lattice structure of the textured Ti_3AlC_2 coating at the substrate/coating interface, and, (d) FFT image of the area marked in (c) by the white square.

IV. Discussion

Highly textured, single-phase and polycrystalline Cr_2AlC, Ti_2AlC and Ti_3AlC_2 MAX phase films have been successfully synthesized via thermal annealing of nanoscale elemental multilayers, irrespective of the substrate type (211 MAX phase coatings of very similar quality and structure were fabricated on amorphous SiO_2/Si substrates and polycrystalline Zr-alloy substrates via the same approach previously [28,29]).

The crystallization onset temperatures identified in this study are consistent with previous findings, i.e. thin film growth of Cr_2AlC is feasible at relatively low temperatures (typically ~550°C or higher) [33,40,49] while that of Ti_2AlC requires intermediate temperatures (~700 °C or higher) [42,43,50]. The synthesis temperatures of the 312 phase (here with focus on Ti_3AlC_2) films are normally above 800°C [42,43]. It has been well acknowledged that nucleation and growth of MAX phase films via PVD are profoundly thermally activated considering their relatively large unit cells. A threshold deposition or annealing temperature is required for a specific MAX phase, depending on the chemical composition and lattice structure, to enable sufficient mobility and energy of the atoms to achieve the desired atomic arrangement [16]. It has been suggested that M and C diffusion in MAX phases are more kinetically favored following the numbered sequence (Group 4 to 6) in the periodic table owing to the consecutively decreasing M–C bonding energy [16]. Thus, the lowest synthesis temperatures are anticipated for Cr_2AlC among the 211 MAX carbides [16,40]. Another alternative argument is that the crystallization onset temperatures of specific MAX phase are closely associated with the thermodynamic stability (or bonding energy) of their counterpart binary carbides. As aforementioned, the formation of an intermediate binary carbide or a solid solution phase is inevitable before the crystallization of highly ordered MAX phase structure. A substantially lower thermodynamic stability of binary chromium carbide than binary titanium carbide has been reported [51]. Consequently, a higher energy barrier has to be overcome with respect to formation of Ti_2AlC (i.e. a higher synthesis temperature needed) than that of Cr_2AlC. Higher-

ordered MAX phase structures (312 and 413) require additionally higher formation temperature due to longer diffusion length needed.

Additionally, the threshold temperatures for the formation of MAX phases via annealing of the nanoscale multilayers of this study are slightly reduced compared to previous investigations [20,42,43]. One reasonable interpretation is that the as-deposited multilayers are one type of energetic material (i.e. reactive multilayers, which generally are composed of numerous metallic bilayers) consisting of well-defined heterogeneous structures and stored chemical energy [52]. The stored chemical energy can be utilized to prompt the growth of a MAX phase during a tailored annealing process. It should be pointed out that both an optimal annealing temperature and duration are required to achieve high crystalline quality of the synthesized coatings for each particular MAX phase. Excessively high annealing temperature and long dwell time will result in oxidation and/or decomposition of the MAX phase coatings, as proved previously [45,46].

Epitaxial or textured growth of single-phase thin films of MAX phases are routinely seen on single crystal substrates, for instance on MgO(111) and Al_2O_3(0001), due to the small mismatch of lattice parameters of specific lattice planes between the film and the substrate [17]. Synthesis of MAX phase films on amorphous or polycrystalline substrates via PVD regularly results in growth of thin films with randomly oriented, polycrystalline microstructure. However, highly basal-plane textured MAX phase films (coatings) were realized in this study irrespective of the substrate type. Based on the microstructure evolution and phase formation revealed by XRD and Raman spectroscopy during/after annealing, the underlying mechanisms for growth of the textured MAX phase carbide coatings are proposed and schematically illustrated in Fig. 11. An intercalation (nucleation-free) scenario together with subsequent vacancy ordering and twinning [44,53,54] characterizes the growth route of the textured MAX phase grains, suggested by the crystallographic orientation relationship as presented in Fig. 11.

The transition metal layers in the as-deposited coatings, as noted before, are crystallographically oriented with their most densely packed lattice plane. Such epitaxial/textural stabilization of individual sublayers with few nanometer thickness (often referred to in so-called superlattice structures) via minimization of the strain energy and interfacial energy has been intensively reported in multilayered thin films [55–57]. During annealing, the aluminum and carbon atoms are more mobile considering their smaller atomic radius and/or lower melting points. Previous publications indicated that Al can readily be incorporated into C-deficient binary carbides (TiC_x, CrC_x or VC_x) to form distorted solid solutions [40,44,58]. Thus, at low and intermediate temperatures diffusion of predominant aluminum and carbon atoms should result in formation of disordered, metastable solid solutions as suggested by the in-situ HTXRD measurements. Growth of the solid solutions rather than a mixture of intermetallic and binary carbide phases during annealing could be energetically favorable in a thermodynamic perspective given that the transition metal and the solid solution phases share structural similarities. No evidence for the formation of intermetallic phases was detected during in-situ HTXRD measurements. However, intermetallic compounds were seen after cooling the metastable solid solutions to room temperature previously [29] and herein, suggesting that they preferably decompose into thermodynamic stable phases under more pronounced equilibrium condition. At elevated temperatures, thermally activated ordering and twinning of the distorted solid solutions occurs, leading to the formation of MAX phase structures [44,53,54,58]. The small misfit of the interplanar spacing between the preferred crystallographic oriented planes of the transition metals (as well as the intermediate solid solution phases [40,44,59]) and the basal planes of the MAX phases, as calculated and displayed in Fig. 11, largely contributes to the growth of basal-plane textured 211 MAX phase carbide coatings. One noticeable evidence is that a TiC(111) seed layer was frequently deposited on single crystal substrates to stimulate the epitaxial growth and improve the crystalline quality of MAX phase thin films initially [60–62]. Additionally,

lower growth rates along the *c*-axis for typical hexagonal crystal structures [63,64] likely further promote the textural growth of the MAX phase films.

With respect to the higher-ordered Ti_3AlC_2 MAX phase, the textured and lower-ordered Ti_2AlC phase formed at intermediate temperature range can initiate templated grain growth of textured Ti_3AlC_2 if sufficiently elevated annealing temperature is reached (Fig. 7). Transformation from a lower-ordered MAX phase to the succeeding thermodynamic stable higher-ordered MAX phase, in both bulk materials and thin films, has been reported in the Ti-C-Al [65,66] and Ti-N-Al [53] systems. For instance, full conversion of a stoichiometric mixture of Ti_2AlC and TiC powder into bulk Ti_3AlC_2 can be readily realized via sintering at elevated temperature (~1400°C) [65]. The transformation mechanism might involve intercalation of a TiC layer into the Ti_2AlC structure concurrently with ordering (since TiC can be viewed as stacking fault in Ti_2AlC [67]) or more complex dissociation and rearrangement of these two phases [65,66]. In addition, direct growth of Ti_3AlC_2 from metastable $(TiAl)C_x$ solid solution phase via ordering and twinning might occur considering the low crystallinity and volume content of the intermediate Ti_2AlC phase formed during in situ annealing. Overall, the structural coordination and the crystallographic orientation relationship among the three phases would certainly facilitate the growth of textured and single-phase Ti_3AlC_2 coatings.

The coatings synthesized via the current two-step approach are composed of platelet-like, elongated crystallites (nanosized grains). This can be attributed to the specific multilayered architecture allowing unimpeded expansion of the grains in the lateral direction parallel to the multilayered stacks (interfaces). A similar crystallite morphology was also reported for annealing of Al/TiN multilayers to synthesize Ti_2AlN MAX phase [31]. A limited grain coarsening effect was observed when extending the annealing time. The strongly textured coatings (parallel oriented) inevitably contain principal low-angle boundaries with low energy (Fig. 10), which reduces the driving force for grain boundary migration and hinders the rapid coalescence of the crystallites during annealing. This unique microstructure

likely features attractive mechanical and physical properties and could be beneficial in some applications of the MAX phase coatings, such as low friction and corrosion-resistant coatings and hydrogen diffusion barriers. The two-step approach offers a tool for tailor-made synthesis of textured and single-phase MAX phase films, both low and high ordered, with fine platelet morphology on various kinds of substrates.

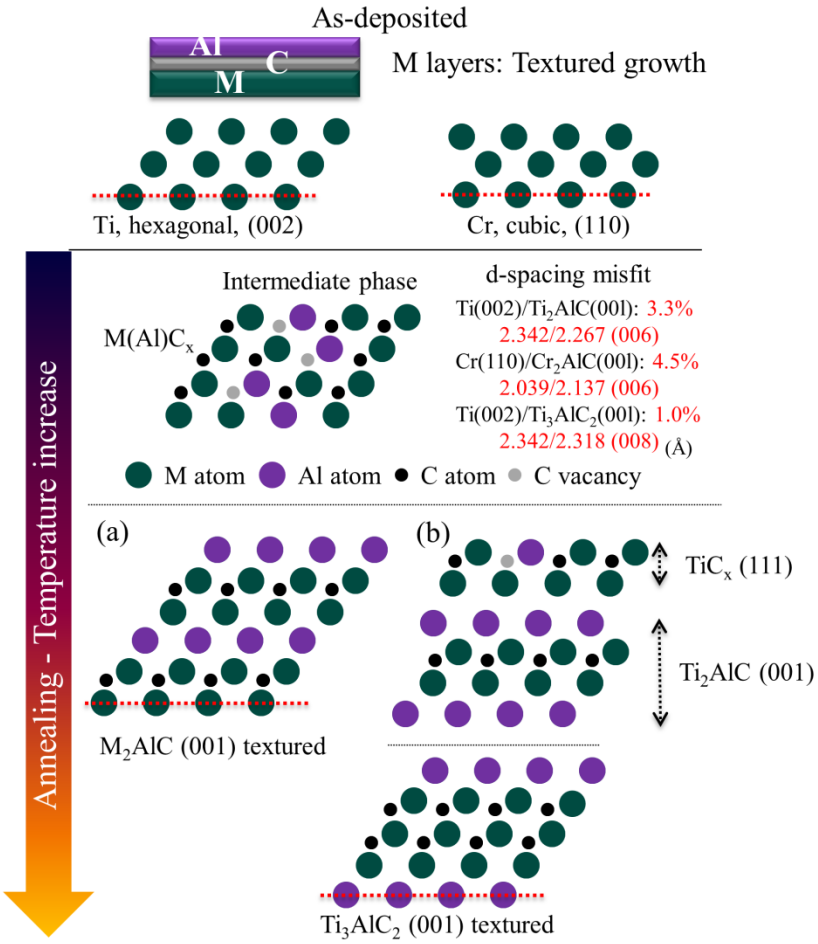

FIG. 11 Proposed schematic illustration of mechanisms for growth of basal-plane textured MAX phase coatings via annealing of M/C/Al reactive multilayers, (a) 211 and (b) 312 MAX phases. Ti_2AlC and TiC_x act as intermediate phases during crystallization of higher-ordered Ti_3AlC_2 phase.

V. CONCLUSIONS

We demonstrated in this study that via controlled thermal annealing of specifically tailored nanoscale multilayers deposited by magnetron sputtering from elemental targets textured and phase-pure MAX phase carbide coatings (Cr_2AlC, Ti_2AlC and Ti_3AlC_2) can be realized on different types of substrates.

The M/C/Al multilayers are composed of amorphous carbon layers and nanocrystalline metallic layers. The transition metal layers are preferred crystallographically oriented with their most densely packed lattice plane, namely Cr (110) and Ti (002) owing to epitaxial/textural stabilization.

Substitutional solid solution carbide phases grow at intermediate temperature range via solid-state diffusion reactions and their subsequent vacancy ordering and twinning result in formation of 211 MAX phase structures during annealing of the multilayers. Lower-ordered Ti_2AlC 211 MAX phase initially crystallized during synthesis of Ti_3AlC_2 312 MAX phase, which likely serve as template as growth of higher-ordered MAX phase. The crystallization onset temperatures were approximately 480°C, 660°C and 820°C for Cr_2AlC, Ti_2AlC and Ti_3AlC_2, respectively.

The structural coordination and the crystallographic orientation relationship among the initial, intermediate and ultimate phases facilitate the growth of textured and single-phase coatings. The unique multilayered architecture in the as-deposited coatings results in the synthesized MAX phase coatings consisting of platelet-like, elongated crystallites.

This novel approach offers prospects for tailor-made synthesis of textured, low- and high- ordered MAX phases with fine platelet morphology on various kinds of substrates and broadens their applications as functional and protective coatings.

ACKNOWLEDGMENTS

The authors thank the Helmholtz (HGF) programs NUSAFE and STN at the Karlsruhe Institute of Technology. C. Tang acknowledges the fellowship supported by the China Scholarship Council (CSC) during his PhD study. The authors also thank Dr. H. Geßwein for HTXRD measurements and Mr. S. Zils, Mr. P. K. Erbes for technical support.

[1] M.W. Barsoum, Prog. Solid State Chem. **28**, 201 (2000).
[2] M.W. Barsoum and M. Radovic, Annu. Rev. Mater. Res. **41**, 195 (2011).
[3] M. Magnuson and M. Mattesini, Thin Solid Films **621**, 108 (2017).
[4] M. Radovic and M.W. Barsoum, Am. Ceram. Soc. Bull. **92**, 20 (2013).
[5] D.J. Tallman, B. Anasori, and M.W. Barsoum, Mater. Res. Lett. **1**, 115 (2013).
[6] D.J. Tallman, L. He, J. Gan, E.N. Caspi, E.N. Hoffman, and M.W. Barsoum, J. Nucl. Mater. **484**, 120 (2017).
[7] J. Ward, D. Bowden, E. Prestat, S. Holdsworth, D. Stewart, M.W. Barsoum, M. Preuss, P. Frankel, M.W. Barsoum, D. Bowden, S. Holdsworth, J. Ward, P. Frankel, and D. Stewart, Corros. Sci. **139**, 444 (2018).
[8] J.L. Smialek, J.A. Nesbitt, T.P. Gabb, A. Garg, and R.A. Miller, Mater. Sci. Eng. A **711**, 119 (2018).
[9] G.L. Messing, S. Poterala, Y. Chang, T. Frueh, E.R. Kupp, B.H. Watson, R.L. Walton, M.J. Brova, A.K. Hofer, R. Bermejo, and R.J. Meyer, J. Mater. Res. **32**, 3219 (2017).
[10] M. Higashi, S. Momono, K. Kishida, N.L. Okamoto, and H. Inui, Acta Mater. **161**, 161 (2018).
[11] X. Duan, L. Shen, D. Jia, Y. Zhou, S. van der Zwaag, and W.G. Sloof, J. Eur. Ceram. Soc. **35**, 1393 (2015).
[12] Y. Liu, Y. Li, F. Li, H. Cui, Y. Pu, S. Guo, and Z. Shi, Scr. Mater. **136**, 55 (2017).
[13] H.B. Zhang, C.F. Hu, K. Sato, S. Grasso, M. Estili, S.Q. Guo, K. Morita, H. Yoshida, T. Nishimura, T.S. Suzuki, M.W. Barsoum, B.N. Kim, and Y. Sakka, J. Eur. Ceram. Soc. **35**, 393 (2015).
[14] T. Lapauw, K. Vanmeensel, K. Lambrinou, and J. Vleugels, Scr. Mater. **111**, 98 (2016).
[15] C. Hu, Y. Sakka, S. Grasso, T. Nishimura, S. Guo, and H. Tanaka, Scr. Mater. **64**, 765 (2011).
[16] P. Eklund, M. Beckers, U. Jansson, H. Högberg, and L. Hultman, Thin Solid Films **518**, 1851 (2010).
[17] A.S. Ingason, A. Petruhins, and J. Rosen, Mater. Res. Lett. **4**, 152 (2016).
[18] M. Sonestedt, J. Frodelius, M. Sundberg, L. Hultman, and K. Stiller, Corros. Sci. **52**, 3955 (2010).
[19] C. Walter, D.P. Sigumonrong, T. El-Raghy, and J.M. Schneider, Thin Solid Films **515**, 389 (2006).
[20] Q.M. Wang, A. Flores Renteria, O. Schroeter, R. Mykhaylonka, C. Leyens, W. Garkas, and M. to Baben, Surf. Coatings Technol. **204**, 2343 (2010).
[21] J.J. Li, M.S. Li, H.M. Xiang, X.P. Lu, and Y.C. Zhou, Corros. Sci. **53**, 3813 (2011).
[22] R. Shu, F. Ge, F. Meng, P. Li, J. Wang, Q. Huang, P. Eklund, and F. Huang, Vacuum **146**, 106 (2017).
[23] S. Gupta, D. Filimonov, T. Palanisamy, and M.W. Barsoum, Wear **265**, 560 (2008).
[24] Y. Du, J.-X. Liu, Y. Gu, X.-G. Wang, F. Xu, and G.-J. Zhang, Ceram. Int. **43**, 7166 (2017).

[25] N. Li, R. Sakidja, and W.Y. Ching, Jom **65**, 1487 (2013).
[26] C. Xu, H. Zhang, S. Hu, X. Zhou, S. Peng, H. Xiao, and G. Zhang, J. Nucl. Mater. **488**, 261 (2017).
[27] F. Colonna and C. Elsässer, RSC Adv. **7**, 37852 (2017).
[28] C. Tang, M.K. Grosse, P. Trtik, M. Steinbrück, M. Stüber, and H.J. Seifert, Acta Polytech. **58**, 69 (2018).
[29] C. Tang, M. Klimenkov, U. Jaentsch, H. Leiste, M. Rinke, S. Ulrich, M. Steinbrück, H.J. Seifert, and M. Stueber, Surf. Coatings Technol. **309**, 445 (2017).
[30] C. Tang, M. Steinbrueck, M. Stueber, M. Grosse, X. Yu, S. Ulrich, and H.J. Seifert, Corros. Sci. **135**, 87 (2018).
[31] L. Gröner, L. Kirste, S. Oeser, A. Fromm, M. Wirth, F. Meyer, F. Burmeister, and C. Eberl, Surf. Coatings Technol. **343**, 166 (2018).
[32] M. Hopfeld, R. Grieseler, T. Kups, M. Wilke, and P. Schaaf, Adv. Eng. Mater. **15**, 269 (2013).
[33] R. Grieseler, B. Hähnlein, M. Stubenrauch, T. Kups, M. Wilke, M. Hopfeld, J. Pezoldt, and P. Schaaf, Appl. Surf. Sci. **292**, 997 (2014).
[34] B. Tsaur, M.S. DiIorio, and A.J. Strauss, Appl. Phys. Lett. **51**, 958 (1987).
[35] C. Tang, Synthesis and High-Temperature Oxidation of Ternary Carbide Coatings on Zirconium-Based Alloy Cladding, 2019.
[36] J.L. Smialek, J. Eur. Ceram. Soc. **37**, 23 (2017).
[37] S. Li, G. Song, K. Kwakernaak, S. van der Zwaag, and W.G. Sloof, J. Eur. Ceram. Soc. **32**, 1813 (2012).
[38] H. Zhang, T. Hu, Z. Li, Y. Zhang, M. Hu, X. Wang, and Y. Zhou, J. Am. Ceram. Soc. **7**, 1 (2016).
[39] M. Baben, L. Shang, J. Emmerlich, and J.M. Schneider, Acta Mater. **60**, 4810 (2012).
[40] A. Abdulkadhim, M. to Baben, T. Takahashi, V. Schnabel, M. Hans, C. Polzer, P. Polcik, and J.M. Schneider, Surf. Coatings Technol. **206**, 599 (2011).
[41] O. Berger, C. Leyens, S. Heinze, R. Boucher, and M. Ruhnow, Thin Solid Films **580**, 6 (2015).
[42] O. Wilhelmsson, J.-P. Palmquist, E. Lewin, J. Emmerlich, P. Eklund, P.O.Å. Persson, H. Högberg, S. Li, R. Ahuja, O. Eriksson, L. Hultman, and U. Jansson, J. Cryst. Growth **291**, 290 (2006).
[43] O. Wilhelmsson, J.-P. Palmquist, T. Nyberg, and U. Jansson, Appl. Phys. Lett. **85**, 1066 (2004).
[44] A. Abdulkadhim, T. Takahashi, D. Music, F. Munnik, and J.M. Schneider, Acta Mater. **59**, 6168 (2011).
[45] M. Beckers, N. Schell, R.M.S. Martins, A. Mücklich, and W. Möller, Appl. Phys. Lett. **89**, 074101 (2006).
[46] J. Emmerlich, D. Music, P. Eklund, O. Wilhelmsson, U. Jansson, J.M. Schneider, H. Högberg, and L. Hultman, Acta Mater. **55**, 1479 (2007).
[47] J. Wang, Y. Zhou, Z. Lin, F. Meng, and F. Li, Appl. Phys. Lett. **86**, 101902 (2005).
[48] V. Presser, M. Naguib, L. Chaput, A. Togo, G. Hug, and M.W. Barsoum, J. Raman Spectrosc. **43**, 168 (2012).
[49] J.J. Li, Y.H. Qian, D. Niu, M.M. Zhang, Z.M. Liu, and M.S. Li, Appl. Surf. Sci. **263**, 457 (2012).
[50] Y. Li, G. Zhao, Y. Qian, J. Xu, and M. Li, Vacuum **153**, 62 (2018).
[51] S.R. Shatynski, Oxid. Met. **13**, 105 (1979).
[52] D.P. Adams, Thin Solid Films **576**, 98 (2015).
[53] I.C. Schramm, C. Pauly, M.P. Johansson Jõesaar, P. Eklund, J. Schmauch, F. Mücklich, and M. Odén, Acta Mater. **129**, 268 (2017).
[54] D.P. Riley and E.H. Kisi, J. Am. Ceram. Soc. **90**, 2231 (2007).

[55] Y.X. Xu, L. Chen, F. Pei, K.K. Chang, and Y. Du, Acta Mater. **130**, 281 (2017).
[56] Q. Guo and G.B. Thompson, Acta Mater. **148**, 63 (2018).
[57] M. Stueber, H. Holleck, H. Leiste, K. Seemann, S. Ulrich, and C. Ziebert, J. Alloys Compd. **483**, 321 (2009).
[58] A. Abdulkadhim, M. To Baben, V. Schnabel, M. Hans, N. Thieme, C. Polzer, P. Polcik, and J.M. Schneider, Thin Solid Films **520**, 1930 (2012).
[59] Y. Zhou and Z. Sun, Mater. Res. Innov. **3**, 286 (2006).
[60] H. Högberg, P. Eklund, J. Emmerlich, J. Birch, and L. Hultman, J. Mater. Res. **20**, 779 (2005).
[61] J. Rosen, P.O.Å. Persson, M. Ionescu, A. Kondyurin, D.R. McKenzie, and M.M.M. Bilek, Appl. Phys. Lett. **92**, 064102 (2008).
[62] M. Magnuson, L. Tengdelius, G. Greczynski, F. Eriksson, J. Jensen, J. Lu, M. Samuelsson, P. Eklund, L. Hultman, and H. Högberg, J. Vac. Sci. Technol. A **37**, 021506 (2019).
[63] Y. Zhou and Z. Sun, Mater. Res. Innov. **2**, 360 (1999).
[64] J. Emmerlich, H. Högberg, S. Sasvári, P.O.. Persson, L. Hultman, J.P. Palmquist, U. Jansson, J.M. Molina-Aldareguia, and Z. Czigány, J. Appl. Phys. **96**, 4817 (2004).
[65] E.H. Kisi, E. Wu, J.S. Zobec, J.S. Forrester, and D.P. Riley, J. Am. Ceram. Soc. **90**, 1912 (2007).
[66] E. Wu and E. Herold Kisi, J. Am. Ceram. Soc. **89**, 710 (2006).
[67] D.J. Tallman, L. He, B.L. Garcia-Diaz, E.N. Hoffman, G. Kohse, R.L. Sindelar, and M.W. Barsoum, J. Nucl. Mater. **468**, 194 (2016).